Journal of
Synchrotron Radiation

ISSN 0909-0495

addenda and errata

Reciprocal space mapping and single-crystal scattering rods. Erratum

Detlef-M. Smilgies,[a]* Daniel R. Blasini,[a,b] Shu Hotta[c] and Hisao Yanagi[d]

[a]CHESS Center, Cornell University, Ithaca, NY 14853, USA, [b]Department of Chemistry and Chemical Biology, Cornell University, Ithaca, NY 14853, USA, [c]Department of Polymer Science and Engineering, Kyoto Institute of Technology, Matsugasaki, Sakyo-ku, Kyoto 606-8585, Japan, and [d]Faculty of Engineering, Kobe University, Rokkodai, Nada-ku, Kobe 657-8501, Japan. E-mail: dms79@cornell.edu

While assembling the high-resolution graphics for Fig. 2 of Smilgies *et al.* [*J. Synchrotron Rad.* (2005). **12**, 807–811], the curve from the bottom panel was erroneously repeated in the top panel. Below is the corrected figure.

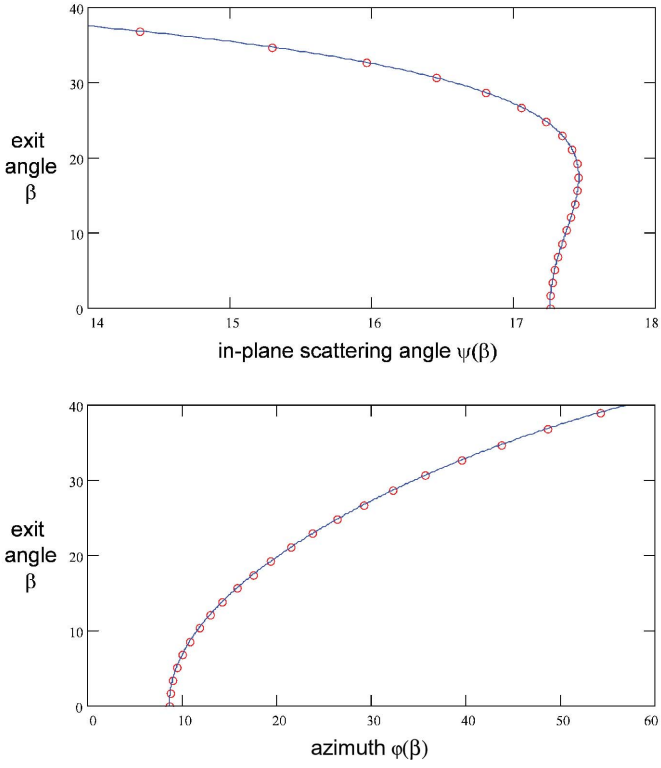

Figure 2
Exit-angle dependence of the scattering angle ψ (top panel) and the sample azimuth φ (bottom panel). Solid lines, based on equations (5*a*) and (5*b*), respectively, were compared with angular calculations (dots) using the *sixc* diffractometer code (Lohmeier & Vlieg, 1993). Axes were chosen such that they correspond to the experimental scattering intensity maps.

References

Lohmeier, M. & Vlieg, E. (1993). *J. Appl. Cryst.* **26**, 706–716.

  doi:10.1107/S0909049506015810

Journal of
Synchrotron Radiation

ISSN 0909-0495

Received 16 July 2005
Accepted 26 September 2005

Reciprocal space mapping and single-crystal scattering rods

Detlef-M. Smilgies,[a]* Daniel R. Blasini,[a,b] Shu Hotta[c] and Hisao Yanagi[d]

[a]CHESS Center, Cornell University, Ithaca, NY 14853, USA, [b]Department of Chemistry and Chemical Biology, Cornell University, Ithaca, NY 14853, USA, [c]Department of Polymer Science and Engineering, Kyoto Institute of Technology, Matsugasaki, Sakyo-ku, Kyoto 606-8585, Japan, and [d]Faculty of Engineering, Kobe University, Rokkodai, Nada-ku, Kobe 657-8501, Japan. E-mail: dms79@cornell.edu

Reciprocal space mapping using a linear gas detector in combination with a matching Soller collimator has been applied to map scattering rods of well oriented organic microcrystals grown on a solid surface. Formulae are provided to correct image distortions in angular space and to determine the required oscillation range, in order to measure properly integrated scattering intensities.

Keywords: grazing-incidence diffraction; scattering rods; reciprocal space mapping.

1. Introduction

Owing to the current strong interest in self-organized molecular films and supramolecular assemblies, an efficient scattering technique is needed to analyze crystalline order and preferential orientation in such systems. Reciprocal space mapping under grazing incidence (GI-RSM) provides easy-to-use charting of large portions of reciprocal space to look for often unknown structures.

GI-RSM using a combination of a Soller collimator and a position-sensitive detector (PSD) with matching large apertures of typically 100 to 200 mm was originally introduced to study molecular self-organization at the air–water interface (for a review see Als-Nielsen *et al.*, 1994). In this case molecules form two-dimensional powders, *i.e.* they have a well defined orientation perpendicular to the water surface, while there is no lateral preferred orientation owing to the disordered nature of the liquid substrate. Hence essentially 2θ powder scans are taken with the scattering intensity perpendicular to the surface recorded by the PSD.

The method can be easily extended to solid systems of molecules absorbed on glass or on silicon wafers. However, using single crystalline substrates, that may induce lateral preferential orientations in the molecular film, poses an extra challenge of keeping track of the scattering rods (Feidenhans'l, 1989) in non-linear angular space. For point detectors, the so-called z-axis scattering geometry is well documented (Bloch, 1985; Feidenhans'l, 1989; Lohmeier & Vlieg, 1993) and various diffractometer codes are readily available. We will give a simple geometric interpretation of the z-axis scattering geometry, and discuss the implications for applying GI-RSM to single-crystalline systems.

2. Geometric analysis of surface scattering

For surface scattering it is mandatory to use the grazing-incidence scattering geometry. First of all, a better signal-to-noise ratio for weak scattering systems is obtained, as the penetration of the X-ray beam into the substrate, and hence diffuse scattering from the bulk, can be greatly reduced. As a convenient side effect, the power density of the incident beam is decreased at grazing incidence, and radiation damage, a major issue for organic materials, is reduced (Smilgies *et al.*, 2002). The natural scattering angles in surface scattering are given by the incident angle α, the in-plane scattering angle ψ, and the exit angle β (Bloch, 1985; Smilgies, 2002). Furthermore, the sample azimuth φ needs to be adjustable in order to match up the in-plane scattering vector with the sample reciprocal lattice. With these four scattering angles, any point of reciprocal space within the Ewald sphere can be reached.

Fig. 1 shows the Ewald construction for surface scattering, for the case $\alpha = 0$. For an in-plane reflection with the scattering vector $\mathbf{Q}$ parallel to the surface, the in-plane scattering angle ψ and the azimuth angle φ can be obtained, as usual, from the scattering triangle,

$$\begin{aligned} \mathbf{Q} &= \mathbf{K}_\mathrm{f} - \mathbf{K}_\mathrm{i}, \\ Q &= 2k\sin(\psi_0/2) = 2k\sin(\varphi_0). \end{aligned} \tag{1}$$

$\mathbf{K}_\mathrm{i}$ and $\mathbf{K}_\mathrm{f}$ are the projections of the incident and exit wavevectors $\mathbf{k}_\mathrm{i}$ and $\mathbf{k}_\mathrm{f}$ onto the sample surface for incident and exit angles α and β, respectively.

$$\begin{aligned} K_\mathrm{i} &= k\cos(\alpha), \\ K_\mathrm{f} &= k\cos(\beta), \end{aligned} \tag{2}$$

and $k = 2\pi/\lambda$ is the vacuum wavevector for X-rays with wavelength λ.

As we move up the scattering rod, the length of the vertical projection k_fz increases at the expense of the in-plane component $\mathbf{K}_\mathrm{f}$, while the in-plane scattering vector $\mathbf{Q}$ has to keep a fixed length to stay on the scattering rod. This is only possible if $\mathbf{Q}$ rotates towards $\mathbf{K}_\mathrm{i}$. Thus the path through angular space corresponds to the intersection of the Ewald

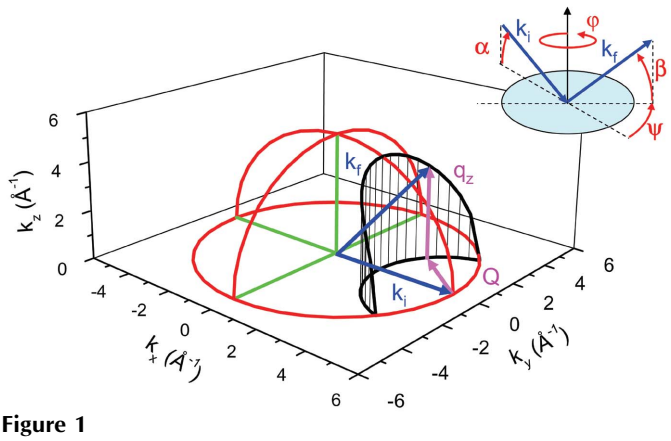

Figure 1
Ewald construction for a rod scan, as used in grazing-incidence diffraction. The top inset displays the four relevant scattering angles α, ψ, β and φ, while the bottom figure shows the scattering vectors and the Ewald sphere. When the exit wavevector $\mathbf{k}_f$ moves up a scattering rod, it has to follow the intersection of the Ewald sphere with a cylinder defined by the requirement that the length of the in-plane scattering vector $\mathbf{Q}$ stays fixed. The incident wavevector $\mathbf{k}_i$ was chosen parallel to the surface for convenience; however, the formulae provided in the text cover the general situation.

sphere of radius k with a cylinder centered around the tip of $\mathbf{K}_i$ with radius Q (see Fig. 1).

Despite this complexity, we can parameterize the path in angular space as a function of the exit angle β in a straightforward way. When the exit wavevector $\mathbf{k}_f$ moves up the scattering rod, its in-plane projection $\mathbf{K}_f$ becomes shorter, and has to move towards $\mathbf{K}_i$ to maintain a fixed length of $\mathbf{Q}$. As $\mathbf{Q}$ has to rotate in the process, both the sample azimuth φ and the in-plane scattering vector ψ have to rotate along. From Fig. 1 it can be seen that the rotation of $\mathbf{K}_f$ and of $\mathbf{Q}$ can be calculated by applying the cosine theorem,

$$\cos(\psi) = \left(K_i^2 + K_f^2 - Q^2\right)/\left(2K_iK_f\right), \qquad (3a)$$

$$\cos(\eta) = \left(K_i^2 + Q^2 - K_f^2\right)/\left(2K_iQ\right), \qquad (3b)$$

where the angle between $\mathbf{K}_i$ and $\mathbf{Q}$ is denoted η. For in-plane scattering ($\alpha = \beta = 0$) we have $\eta = 90^\circ - \varphi_0$, where the in-plane Bragg angle φ_0 was defined in (1). The sample azimuth φ at arbitrary β is thus given by

$$\varphi = 90^\circ - \eta. \qquad (4)$$

Expressing the scattering condition in terms of the scattering angles finally yields

$$\cos(\psi) = \left[\cos^2(\alpha) + \cos^2(\beta) - 4\sin^2(\varphi_0)\right]/\left[2\cos(\alpha)\cos(\beta)\right], \qquad (5a)$$

$$\sin(\varphi) = \sin(\varphi_0) + \left[\cos^2(\alpha) - \cos^2(\beta)\right]/\left[4\cos(\alpha)\sin(\varphi_0)\right]. \qquad (5b)$$

Two types of maps of the scattering intensity are interesting: (i) a radial map $I(\psi, \beta)$ for a specific sample azimuth and (ii) an orientational map $I(\Delta\varphi, \beta)$ at a fixed in-plane scattering vector. The radial map shows the molecular reflections as a function of parallel scattering vector $\mathbf{Q}$ along a specific high-symmetry direction of the substrate. For an orientation map,

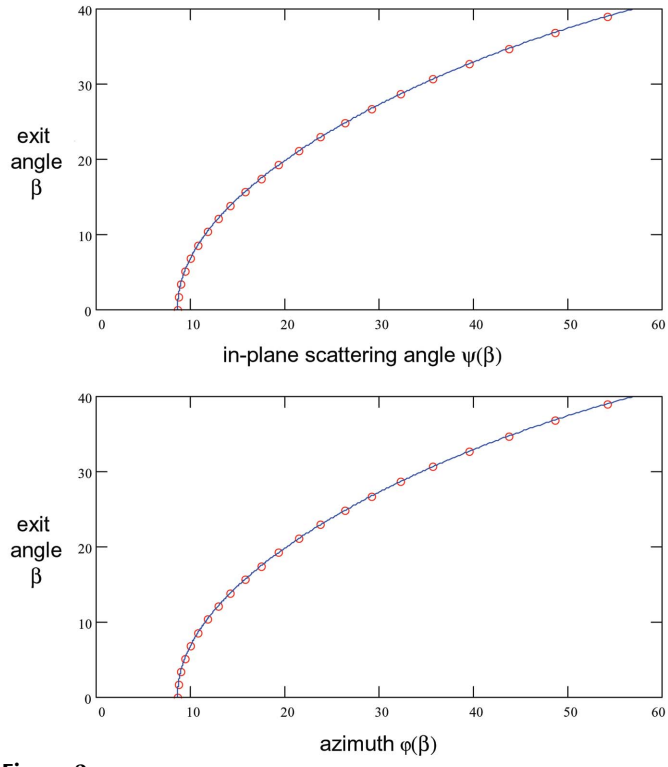

Figure 2
Exit-angle dependence of the scattering angle ψ (top panel) and the sample azimuth φ (bottom panel). Solid lines based on equations (5*a*) and (5*b*), respectively, were compared with angular calculations (dots) using the *sixc* diffractometer code (Lohmeier & Vlieg, 1993). Axes were chosen such that they correspond to the experimental scattering intensity maps.

which can be considered as the surface scattering analogue of a pole figure scan, we have to undo the distortion of the orientation map at higher β given by (5*b*). $\Delta\varphi$ denotes the angular deviation from a specific substrate direction [*uvw*] in the surface plane. Both angular functions are illustrated in Fig. 2 assuming an X-ray wavelength of 1.2 Å and an in-plane scattering vector $\mathbf{Q}$ of 1.5 Å, which are a typical values for studies of organic systems.

Moreover, we cannot just simply scan ψ (as is possible in a powder scan) or φ for a single-crystalline sample, as φ and ψ turned out to be dependent on β *simultaneously*. In order to obtain accurate integrated intensities throughout the exit-angle range covered by the PSD, we have to oscillate the other angular axis during the scan, so that it is ensured that the scattering conditions are met all along the section of the rod covered by the detector. Thus φ should oscillate, while recording a radial map $I(\psi, \beta)$. Similarly, while measuring the orientation map $I(\Delta\varphi, \beta)$, we should apply an oscillation to ψ. The required oscillation ranges can be determined from (5*a*) and (5*b*) and Fig. 2, taking into account the finite exit-angle range accepted by the detector system and the collimator resolution.

The formulae described remain valid for an area detector covering an in-plane scattering range (ψ) as well as an exit-angle range (β). Note that the azimuth oscillation (φ) is still necessary when dealing with single crystalline samples (see for instance Liu *et al.*, 2005). The approach described above has

some advantages over detection using an area detector. First of all, molecular scattering is often weak and diffuse, and it pays off to have a single-photon-counting detector which is essentially free of electronic noise. This is not the case with common area detectors based on charge-coupled devices. A second factor improving signal-to-noise in the described scheme is the one-dimensional collimation provided by the Soller collimator which helps to reduce the diffuse scattering background from the sample. Moreover, a collimator defining the scattering angle allows the use of a large detection area on the sample which helps to spread out the X-ray flux density on the sample and thus to reduce radiation damage. A collimation-free area detector, as in a standard protein crystallography set-up, would need a relatively small illuminated spot to reduce angular smearing. Ultimately the choice of detector systems remains a function of the particular system studied and detector availability.

3. Experimental application

As an application example we present data for 2,5-bis(4-biphenyl)thiophene (BP1T) grown on KCl (001) substrates by organic vapor deposition. It was found that BP1T forms distinct microcrystallites on KCl (001) (Yanagi *et al.*, 2001). The molecule has been noted for its optical fluorescence and electrofluorescence properties making it a candidate material for blue organic light-emitting diodes (Yanagi *et al.*, 2001, 2003). BP1T is a boomerang-shaped molecule that grows in the $P2_1/n$ monoclinic space group with lattice constants a = 7.608 Å, b = 5.8219 Å, c = 43.76 Å and β = 93.51° (Hotta & Goto, 2002). Synthesis and purification methods have been described by Hotta *et al.* (2000).

X-ray scattering experiments were performed at the CHESS G2 station (Smilgies, Clasby *et al.*, 2005) featuring an X-ray transparent Be(0002) side-bounce monochromator/beam splitter that deflects a 0.1% bandwidth slice from the intense multilayer beam generated by the G-line 50-pole wiggler and the doubly focused main G-line optics. The incident beam with an X-ray wavelength of 1.464 Å was collimated vertically to 0.2 mm using a set of two slits, while the full horizontal beam width of about 5 mm was accepted. Samples were mounted horizontally and the incidence angle was set to 0.2°. Data were taken with a horizontal four-circle diffractometer and a six-circle kappa diffractometer supporting a large Soller collimator (JJ X-ray) and a position-sensitive linear gas detector (ORDELA) with matching apertures of 8 mm horizontal and 100 mm vertical. The complete G2 GI-RSM system is depicted in Fig. 3.

The new six-circle kappa diffractometer at the G2 station features a two-component detector arm which allows the β-range to be extended by tilting the vertical arm by an angle γ. Hence an exit-angle range from $\gamma + \beta_{\rm min}$ to $\gamma + \beta_{\rm max}$ can be covered augmenting the grazing-exit map. Applying (5*a*) and (5*b*) will help to keep the diffractometer on track.

Samples were lined up by first using the reflection of a laser beam and a manual sample goniometer, in order to ensure that the sample normal was parallel to the φ axis of the azimuth rotation. The incident angle was set after aligning the sample parallel to the incident X-ray beam. The in-plane azimuth direction was then calibrated by lining up on the KCl (220) in-plane reflection, and setting the corresponding φ angle to φ_0. A radial scan thus corresponds to a φ–ψ scan with $\varphi = \psi/2$. While collecting data, an appropriate oscillation had to be applied to φ, as discussed above.

BP1T features a polymorph three-dimensional growth on KCl (001) and forms both microscopic platelets and needles with bulk structure (Smilgies, Blasini *et al.*, 2005). Both types of structures display their signatures in a $I(\psi, \beta)$ map along the [110] substrate high-symmetry direction (Fig. 4). The series of streaks in the ψ direction can be identified as the (00L) series with L = 2, 4, . . . , 10 characteristic of needles with the long molecular axis parallel to the surface, *i.e.* lying molecules. The scattering rod marked (11L) shows a series of closely spaced reflections in the vertical direction indicating standing molecules which form platelets (Yanagi *et al.*, 2001, 2003). In order to provide accurate integrated intensities, as discussed above, the sample was oscillated by ±7° during data acquisition.

The angular map can be transformed into a reciprocal space map for further analysis by the transformation

$$\begin{aligned} Q &= k\big[\cos 2(\alpha) - 2\cos(\alpha)\cos(\varphi)\cos(\beta) + \cos 2(\beta)\big]^{-1/2} \\ q_z &= k\big[\sin(\alpha) + \sin(\beta)\big] \end{aligned} \qquad (6)$$

where the parallel component Q of the scattering vector is aligned along the [110] substrate direction. Using the Busing & Levy (1967) transformation, the scattering vector $\mathbf{q} = (\mathbf{Q}, q_z)$ can be transformed into index space (HKL). The in-plane indices H and K are a function of the in-plane azimuth chosen (in our case $H = K = Q/a^*2^{1/2}$, with a^* being the bulk reciprocal lattice vector of the KCl substrate), while L can simply be obtained from $L = q_z/c^*$, where c^* is the reciprocal lattice vector perpendicular to the surface ($c^* = a^*$ in our

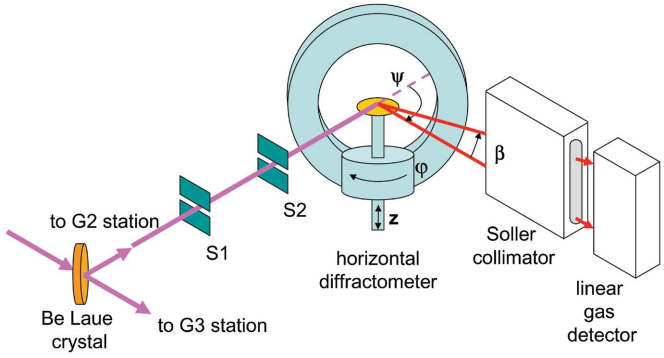

Figure 3
Reciprocal space mapping set-up at the G2 station. A 0.1% bandwidth slice of the intense beam from the G-line 50-pole wiggler and multilayer monochromator is deflected into the G2 station by a Be single-crystal beam splitter. The incident beam is collimated vertically by slits S1 and S2, while the full horizontal beam width of about 5 mm is accepted. The horizontal diffractometer has a motorized sample height stage to precisely align the sample surface into the beam. The scattered beam is detected by a linear gas detector after passing a Soller collimator. Collimator and detector have matching apertures of 8 mm horizontal by 100 mm vertical.

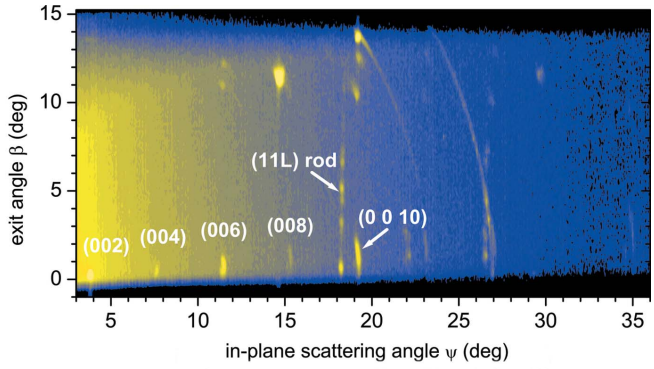

Figure 4
Structure map $I(\psi, \beta)$ as recorded in a radial scan along the KCl [110] high-symmetry direction. Proper integrated intensities were obtained by a $\pm 7^\circ$ oscillation during data acquisition. The $(00L)$ reflection series is due to lying molecules forming needle-like crystallites, while the $(11L)$ rod signifies standing molecules forming platelets. Ring-like structures are three-dimensional powder rings owing to substrate material or unoriented molecular crystallites.

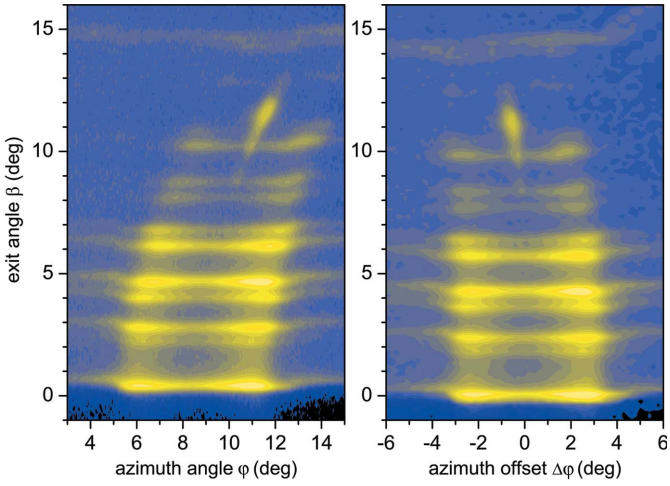

Figure 5
Orientational map $I(\Delta\varphi, \beta)$. Left panel: data as recorded. Right panel: data corrected for distortion. A residual small distortion left in the corrected image may be due to some small sample or detector misalignment. The data clearly show that the BP1T $(11L)$ scattering rods are rotated by 2.5° from the KCl [110] direction. At higher scattering angles there seems to be also evidence for an aligned component. The doublet structure of the BP1T reflections along the scattering rods is caused by monoclinic splitting owing to the existence of 180° domains, as described by Smilgies *et al.* (2000).

case). In principle, either the substrate lattice or the molecular lattice can be used as a reference. We have used the former to characterize epitaxic properties of molecular microcrystallites (Smilgies *et al.*, 2000; Smilgies, 2002). The molecular lattice would be suitable for crystallography of unknown molecule structures and the use of crystallographic indexing methods may be indicated.

As a second example we show the orientational map of the $(11L)$ scattering rod in Fig. 5. The left panel of Fig. 5 shows the map as measured, the right panel the corrected map plotting the deviation of the azimuth angle offset $\Delta\varphi$ from the [110] high-symmetry direction of the substrate.

Examining Fig. 2 (top panel) shows that $\psi(\beta)$ shifts by about 0.2° between $\beta = 0$ and $\beta = 10^\circ$ which corresponds to the exit-angle acceptance of the G2 RSM system. In this case we have to examine the angular resolution of the collimator, as given by the incident beam divergence and the angular acceptance of the Soller collimator. From a measurement of the direct beam we obtained that the in-plane angular resolution was 0.2°, and hence the orientational map was already properly integrated without ψ oscillation. Larger ψ deviations occur at higher exit angles β (see Fig. 2) though, and in such cases ψ should be oscillated.

A small distortion remained in the corrected map (see Fig. 5), which may be due to minor line-up errors. For once, the exact incident angle for cleaved KCl substrates is difficult to determine. While such crystals feature well ordered crystalline terraces of 100 nm or more, the cleavage can result in macroscopic steps at the surface. This is evident from broad and distorted reflections of a laser beam from the surface during line-up. Moreover, owing to the three-dimensional growth of the organic material corresponding to a large microscopic roughness, the X-ray reflectivity from these surfaces is very weak, and cannot be used for line-up. Another possible experimental problem could be a small tilt of the collimator from the vertical direction. For the distortion correction we used the experimentally determined in-plane Bragg angle φ_0 of 8.4° and a nominal incident angle α of 0.5° based on the laser line-up in equation (5*b*).

The orientational map $I(\Delta\varphi, \beta)$ shows a characteristic splitting of about 2.5° with respect to the substrate [110] high-symmetry direction. This peculiar behavior may be related to a Novaco-McTague rotation of the molecular platelets which is a well known feature from other van der Waals systems (Novaco & McTague, 1977). The map shows that in addition to the rotated phase there appears to be also a small portion of platelets aligned with the high-symmetry azimuth. As this subtle effect shows up only at higher β, it is easy to miss with a point detector, with which typically only a few selected reflections are scanned (Smilgies *et al.*, 2000, 2002).

4. Discussion

Within an angular space representation of the well known z-axis surface scattering technique, we have provided formulae to analyze scattering intensity maps. Moreover, the oscillation range for the azimuth angle φ during a radial scan as well as the in-plane scattering angle ψ during an azimuth scan can be determined as a function of exit-angle acceptance of the detector system, in order to facilitate accurate integration of the scattering intensities. The example of BP1T crystallites grown on KCl (001) substrates illustrated that subtle effects may be unveiled which could have been easily overlooked in point detector scans on a conventional surface diffractometer.

Hector Abruña, Cornell Department of Chemistry and Chemical Biology, is thanked for his support and encouragement for building and operating the G2 station. Special thanks

to Dave Nowak, Cornell Materials Science and Engineering, and Basil Blanks, Spacemill Industries, for all their work in setting up the new six-circle kappa diffractometer in the G2 hutch. The BP1T material synthesis was carried out in the Harmonized Molecular Materials Center, Tsukuba, Japan, funded by NEDO through the project on Technology for Novel High-Functional Materials (AIST). DRB acknowledges support by a NSF graduate scholarship. Funding for the G2 station by NSF grants DMR 0114094 (G2 side-bounce monochromator) and DMR 0216881 (kappa diffractometer, detector) as well as by the Cornell Center of Materials Research (Soller collimator) is gratefully acknowledged. CHESS is a national user facility operated under NSF/NIH/NIGMS grant DMR-0225180.

References

Als-Nielsen, J., Jacquemain, D., Kjaer, K., Leveiller, F., Lahav, M. & Leiserovitz, L. (1994). *Phys. Rep.* **246**, 251–313.
Bloch, J. M. (1985). *J. Appl. Cryst.* **18**, 33–36.
Busing, W. R. & Levy, H. A. (1967). *Acta Cryst.* **22**, 457–464.
Feidenhans'l, R. (1989). *Surf. Sci. Rep.* **10**, 105–188.
Hotta, S. & Goto, M. (2002). *Adv. Mater.* **14**, 498–501.
Hotta, S., Kimura, H., Lee, S. A. & Tamaki, T. (2000). *J. Heterocycl. Chem.* **37**, 281–286.
Liu, X., Zhang, Y., Goswami, D. K., Okasinski, J. S., Salaita, K., Sun, P., Bedzyk, M. J. & Mirkin, C. A. (2005). *Science*, **307**, 1763–1766.
Lohmeier, M. & Vlieg, E. (1993). *J. Appl. Cryst.* **26**, 706–716.
Novaco, A. D. & McTague, J. P. (1977). *Phys. Rev. Lett.* **38**, 1286–1289.
Smilgies, D.-M. (2002). *Rev. Sci. Instrum.* **73**, 1706–1710.
Smilgies, D.-M., Blasini, D. R., Yanagi, H. & Hotta, S. (2005). To be published.
Smilgies, D.-M., Boudet, N., Struth, B., Yamada, Y. & Yanagi, H. (2000). *J. Cryst. Growth*, **220**, 88–95.
Smilgies, D.-M., Boudet, N. & Yanagi, H. (2002). *Appl. Surf. Sci.* **189**, 24–30.
Smilgies, D.-M., Clasby, B., Blasini, D. R., Nowak, D. E., Abruña, H. D., Baker, S., Brock, J. D., Gruner, S. M. & Freund, A. K. (2005). To be published.
Yanagi, H., Araki, Y., Ohara, T., Hotta, S., Ichikawa, M. & Tanaguchi, Y. (2003). *Adv. Funct. Mater.* **13**, 767–773.
Yanagi, H., Morikawa, T., Hotta, S. & Yase, K. (2001). *Adv. Mater.* **13**, 313–316.